ADVANCED MATERIALS
www.advmat.de

Heterogeneous Structure Omnidirectional Strain Sensor Arrays With Cognitively Learned Neural Networks

Jun Ho Lee, Seong Hyun Kim, Jae Sang Heo, Jee Young Kwak, Chan Woo Park, Insoo Kim, Minhyeok Lee, Ho-Hyun Park, Yong-Hoon Kim, Su Jae Lee, and Sung Kyu Park**

Mechanically stretchable strain sensors gain tremendous attention for bioinspired skin sensation systems and artificially intelligent tactile sensors. However, high-accuracy detection of both strain intensity and direction with simple device/array structures is still insufficient. To overcome this limitation, an omnidirectional strain perception platform utilizing a stretchable strain sensor array with triangular-sensor-assembly (three sensors tilted by 45°) coupled with machine learning (ML) -based neural network classification algorithm, is proposed. The strain sensor, which is constructed with strain-insensitive electrode regions and strain-sensitive channel region, can minimize the undesirable electrical intrusion from the electrodes by strain, leading to a heterogeneous surface structure for more reliable strain sensing characteristics. The strain sensor exhibits decent sensitivity with gauge factor (GF) of ≈8, a moderate sensing range (≈0–35%), and relatively good reliability (3000 stretching cycles). More importantly, by employing a multiclass–multioutput behavior-learned cognition algorithm, the stretchable sensor array with triangular-sensor-assembly exhibits highly accurate recognition of both direction and intensity of an arbitrary strain by interpretating the correlated signals from the three-unit sensors. The omnidirectional strain perception platform with its neural network algorithm exhibits overall strain intensity and direction accuracy around 98% ± 2% over a strain range of ≈0–30% in various surface stimuli environments.

1. Introduction

In recent years, stretchable strain sensors have attracted much interest due to their mechanical stretchability and multiaxial sensing characteristics, posing substantial potentials for emerging electronics such as wearable electronics, healthcare monitoring, and robotic skin/arms.[1–5] The key deterministic parameters such as sensitivity, durability, sensing range, and response time were significantly improved by tremendous efforts of researchers. Notably, many attempts have been carried out to realize highly strain-sensitive composites consisting of metallic nanowires, carbon nanotubes, carbon/metal nanoparticles, and elastomers.[6,7] Along with such material consolidating strategy, a variety of mechanistic device structures (resistive, capacitive, piezoresistive, triboelectric, and piezoelectric types) has been demonstrated to achieve high-performance strain sensors.[8–12] However, most of the conventional strain sensors are only capable of detecting uniaxial strain and lack the ability to determine directional variable motions, limiting their applications in realistic surface stimuli environments such as dynamic human skin motion sensing and human–machine interfaces.

To address this issue, geometrically engineered[13–15] sensor devices composed of multidimensionally stacked channel or cross-shaped detecting electrodes have been introduced.[16,17] These strain sensors are capable of detecting the difference of gauge factor corresponding to different loading directions, successfully exhibiting direction-dependent sensing characteristics. In fact, these newly engineered architectures have been developed to avoid the difficulty to achieve multidirectional strain sensing by employing microscopically isotropic conducting pathways of sensing channel layers, which typically experience identical deformation upon any stimulating direction. Although

J. H. Lee, J. Y. Kwak, M. Lee, H.-H. Park, S. K. Park
School of Electrical and Electronics Engineering
Chung-Ang University
Seoul 06980, Korea
E-mail: skpark@cau.ac.kr

S. H. Kim, C. W. Park, S. J. Lee
Flexible Electronics Research Section
Electronics and Telecommunications Research Institute
Daejeon 34129, Korea
E-mail: leesujae@etri.re.kr

The ORCID identification number(s) for the author(s) of this article can be found under https://doi.org/10.1002/adma.202208184.

DOI: 10.1002/adma.202208184

J. S. Heo, Y.-H. Kim
School of Advanced Materials Science and Engineering
Sungkyunkwan University
Suwon 16419, Korea

J. S. Heo
IT Project Team, Mobile Display Business
Samsung Display
1 Samsung-ro, Giheung-Gu, Yongin-Si 17113, Korea

I. Kim
Department of Medicine
University of Connecticut School of Medicine
Farmington, CT 06030, USA

these advances are noteworthy, unsatisfactory linearity possibly due to complicated and intermixed conducting pathways in channel region could impede reliable determination of strain direction under complex stimulation environments. Moreover, the complexity of device architectures and implementation of channel structure can be problematic for industrial applications. Therefore, beyond the supervised directional sensing approaches with geometrically engineered devices, a new strategy which mimics the biological perception with simple device architectures has been proposed.[18–21] Human sensory systems can detect multi-mixed signals generated by concurrent events and discriminate each event through a behavior-learned cognition process in the brain. Determining the response in the brain has been typically exerted based on past experiences and cognitively learned rehearsal procedures. One of the machine learning algorithms such as multiclass-multioutput neural network algorithms can mimic such neural process of the brain, exerting the rehearsal process by intentionally generated behavioral data. The cognitively learned neural-network computation may further enable determination and discrimination of certain stimulation intensity and direction via the unique recognition and decoupling of the cross-reactive electrical signals from various intermixed stimuli, which may facilitate simplified device architectures with minimized power consumption.[2,22,23]

Here, we demonstrate a simply designed stretchable strain sensor array for detection and perception of both the direction and intensity of strain via cognitively learned neural network algorithm. The strain sensor is composed of a heterogenous surface architecture featured by stretchable poly(dimethylsiloxane) (PDMS) substrate, poly(ethylene terephthalate) (PET) film forming strain insensitive rigid electrode regions, and strain sensing channel region composed of multiwalled carbon nanotube (MWCNT) with carbon black (CB) nanofiller dispersed in PDMS matrix.[7,24,25] The heterogeneous device architecture can minimize the undesirable electrical interruption from electrodes by strain, leading to more reliable strain sensing characteristics. An omnidirectional strain sensor array with triangular-sensor-assembly is demonstrated by arranging three-unit sensors at tilting angles of 45°, to enable direction-dependent sensing characteristics. Furthermore, high-accuracy perception of strain intensity and direction is achieved by employing a ML process based on multiclass–multioutput neural network and classifier model algorithms. This strategy employing the cognitive learning procedure can provide highly accurate detection of strain intensity and direction, validating the facilitation of cognitively learned sensory system for the application of omnidirectional perceptible strain sensors.

2. Results and Discussion

Figure 1a schematically illustrates the biological tactile sensing system which is composed of three major organs. A mechanoreceptor which senses the external stimuli, neurons that transmit the signals, and the brain that recognizes, classifies, and reacts to the stimuli. For mimicking the biological tactile sensory system, a stretchable strain sensor array is constructed with three-unit sensors tilted at angles of 45° as shown in Figure 1b, allowing the determination of strain direction and intensity. Recently, to overcome the limitation of unidirectional strain sensors, a dual-sensor array has been proposed in which the sensors are positioned in horizontal and vertical directions.[18,26] In this case, the effective strain can be calculated by these equation. The strain applied to the sensor in a coordinate system with x^* and y^* axes according to an arbitrary inclined θ is expressed as follows

$$\varepsilon_{x^*} = \left(\frac{\varepsilon_x + \varepsilon_y}{2}\right) + \left(\frac{\varepsilon_x + \varepsilon_y}{2}\right)\cos 2\theta + \frac{\gamma_{xy}}{2}\sin 2\theta \quad (1)$$

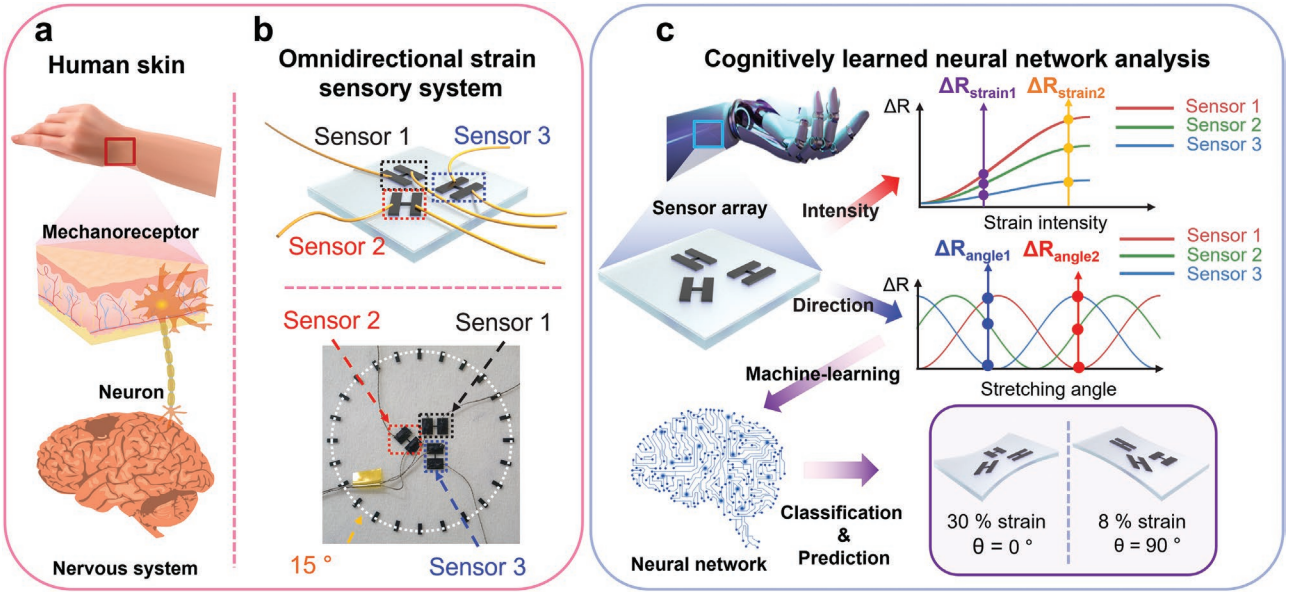

Figure 1. Schematic diagrams of biological sensory system and omnidirectional strain-perceptible sensor array. a) Schematic illustration of the biological tactile sensory system of human, and b) the schematic/photograph of fabricated omnidirectional strain-perceptible sensor array with triangular-sensor-assembly. c) Schematics of cognitively learned neural network analysis process for perception of strain intensity and direction using the omnidirectional strain sensor array.

where γ_{xy} is shear strain. Then, the strain applied to x direction, $\varepsilon_y = \gamma_{xy} = 0$. Therefore, off-axis deformation can be described by $\varepsilon_x = \varepsilon \times \cos^2\theta$, where ε is the applied strain, θ is the angle, and ε_x is the effective strain along the x-axis. Hence, the stretching angle (θ) can be determined by interpreting the measured ε_x.[13–15] However, the dual-sensor array typically shows limited accuracy and only supervised angle determination is possible. In addition, it is theoretically impossible to distinguish between the angles of 70° and 110° due to the symmetrical characteristics of stretching. Therefore, the sensing range is typically limited to ≈0–90° and ≈180–270° (due to the symmetric stretching). It is common to stretch both edges of entire device substrate because a stretching jig automatically measures the strain by fixing one side and pulling the other side. In the same way, when three sensors are used, which are tilted by specific angles, additional axial information can be obtained, enabling omnidirectional (360°) strain sensing. As shown in Figure 1c, with the triangular-shape sensor arrangement, the interpretation of multi-mixed data obtained from three individual sensors is possible, enabling detection of strain intensity and direction compared to the dual-sensor array. Therefore, it is expected that a specific strain intensity and direction can be explored by analyzing the different behaviors of resistance variation (slope) and phase changes of each sensor device, respectively. Moreover, the accuracy of detecting strain intensity and direction with various combinations can be further enhanced by employing ML algorithms mimicking the human neural networks. As a result, when a strain of arbitrary intensity and direction is applied, the omnidirectional strain sensor array can classify and recognize the intensity and direction of strain with high accuracy.

Figure 2a; Figure S2, Supporting Information, shows the device structure and cross-sectional scanning electron microscopy (SEM) image of a unit strain sensor, respectively. The detailed fabrication process of the sensor is described in the Experimental Section; Figure S1, Supporting Information. The strain sensor consists of heterogenous surface regions featured by; electrode regions which are stacked on rigid PET islands and a strain-sensing channel region connecting the two electrode regions. The electrode regions are insensitive to strain due to the bottom PET rigid islands. In contrast, the channel region without the rigid island is sensitive to strain. Therefore, when stretched, the imposed strain mainly affects the strain-sensitive channel region, enabling more accurate strain detection. In our sensor structures, the two parts (sensing channel region and electrodes) are made by same materials and coated simultaneously, ensuring stable electrical contact between the sensing part and electrode part. In addition, detailed tensile strength simulation was performed as described in Figure S3, Supporting Information, to ensure device reliability and verify stability.[27] Therefore, deformation due to the difference in Young's modulus between different materials does not occur. The difference in modulus can be critical weakness in the strain sensor; so, we selected a single-layer rigid island considering the modulus between the substrate and the rigid island. As a result, the sensor shows good contact stability without large slippage up to high strain level. Furthermore, due to the asymmetric channel structure of the sensor device, strain direction can be also identified. Aforementioned, when an arbitrary directional strain ε is applied at an angle of θ, the effective strain that affects the resistance change can be calculated as $\varepsilon_x = \varepsilon \times \cos^2\theta$, whereas, the off-axis deformation can be calculated as $\varepsilon_y = \varepsilon \times \sin^2\theta$ (Figure 2b). Therefore, because the change of the resistance varies according to the applied strain angle, the strain direction can be evaluated by analyzing the resistance variations of the three-unit sensors. Figure 2c illustrates the possible mechanism of strain intensity- and

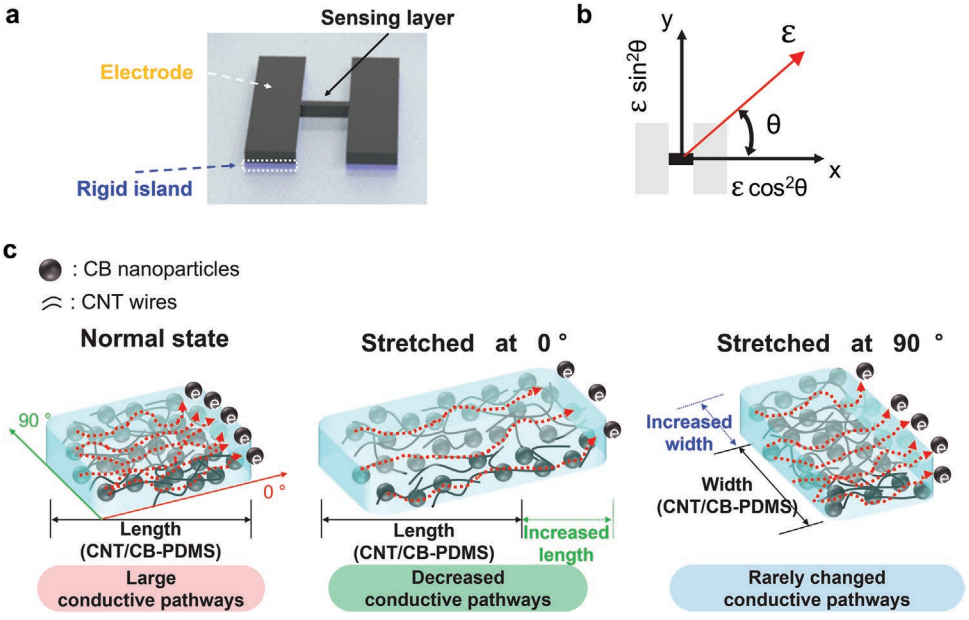

Figure 2. Device structure of fabricated unit strain sensor and the sensing mechanism. a) Schematic structure of the unit strain sensor consisting of strain-insensitive electrode regions and strain-sensitive channel region. b) Schematic of the strain components with respect to x- and y-axis (θ: stretching angle). c) Sensing mechanism of the strain sensor. The length and width of MWCNT/CB-PDMS are subject to change according to the intensity and direction of strain.

direction-dependent resistance variation. At normal state with zero strain, the unit sensor shows a baseline resistance of ≈80 kΩ. Then, when the sensor is stretched at an angle (θ) of 0° (longitudinal direction; strain direction parallel to channel), the number of conducting pathways between MWCNT and CB is decreased. As a result, the resistance tends to increase with the strain level.[28–31] Meanwhile, when the sensor is stretched at an angle of 90° (transversal direction; strain direction perpendicular to channel), the number of conducting pathways between MWCNT and CB is barely changed due to limited elongation along the transversal direction by the two rigid regions. Thus, the resistance change is relatively small. Moreover, when the sensor is stretched at an arbitrary angle between 0° and 90°, the resistance changes according to the level of longitudinal strain applied to the sensor.

In addition, to investigate the effect of device architecture on sensing characteristics, finite element analysis (FEA) was performed as shown in Figure S4, Supporting Information. A comparison of strain sensing performance with and without rigid island was carried out by FEA simulation with strain intensity of 30% at 0°. The structure of three-sensor array was designed with tilting angles of 45° between the sensors. The designed model and the material parameters used for the simulation are listed in Tables S1, Supporting Information. The color legends represent the strain intensity applied to the sensor. As shown in Figure S4b, Supporting Information, the strain experienced by each sensor was highly dependent on the presence of rigid islands. With rigid islands, the strain at the channel region of each sensor was 33.5% (θ = 0°), 23% (45°), and 6.2% (90°), showing an evident angle-dependency. Meanwhile, without the rigid islands, the strain at the channel region was 36% (θ = 0°), 29% (45°), and 21% (90°). As indicated, without the rigid islands, decent sensitivity and accuracy cannot be achieved because the strain is applied evenly across the sensor array. It is to note that with the rigid islands, the strain value at 0° sensor was slightly larger (33.5%) than the applied strain (30%). This can be attributed to two facts. First, the Young's modulus of channel region is much smaller than that of the electrode region. The channel region and electrode region are made by the same material; however, due to the rigid island, they have different strain distributions. Therefore, this can be the prominent factor for the observed high strain. Second, this is attributed to the fact that the channel layer is also stretched slightly to the transversal direction because the analysis method of FEA calculates the total strain of selected region to both transversal and longitudinal direction. In this case, ununiform distribution of slightly larger strain generally occurrs in a small modulus region.[32] Nonetheless, with the rigid islands, clear angle-dependent sensing behavior can be obtained, enabling the omnidirectional strain perception.

To design strain sensor array with highly efficient and stable performance, FEA was also performed as shown in Figure S5, Supporting Information. The various parameters such as channel length, electrode pad size, number, and arrangement of strain sensors were varied, and the final architecture of sensor unit/array was designed. **Figure 3**a summarizes the influence on the difference of strain between applied strain and detected strain in the sensor array versus pad size, channel length, and the excessive local strain applied to the sensor array with different footprints (distance between channel layers). As a result, the design of three-sensor array was optimized as 18 mm^2 of pad size, 1 mm of channel length for minimizing the difference between applied and detected strain. In addition, when the footprint is too small (high density), the device can

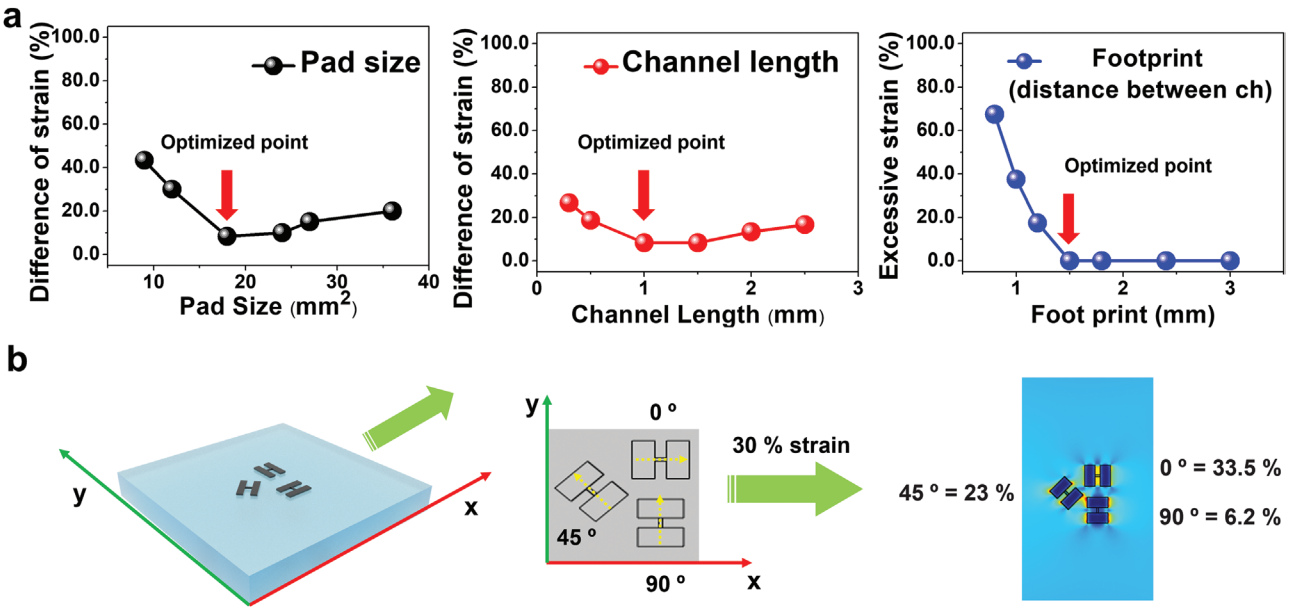

Figure 3. The FEA simulation results of optimized directional strain responses of strain sensor arrays. a) Influence of design parameters on the difference of strain between applied strain and detected strain in the three-sensor array versus pad size (left), channel length (middle), and excessive local strain (right) applied to the sensor array with different footprints (distance between channel layers). b) Schematic of three-sensor array (left), top-view of sensor array arranged with three-unit sensors tilted at 45° (middle), and the FEA simulation results (right). The strain at the channels was analyzed as 33.5% (0°), 23% (45°), and 6.2% (90°).

be easily destroyed because of sharp excessive strain applied to the edge point. As a result, the length between each channel was designed as 1.5 mm showing the lowest peak strain with minimum array size. Therefore, it can be confirmed that stable and precise detection is possible in the sensing layer. Based on these results, we optimized the structure and size of the strain sensor array. In addition, the FEA simulation structures and result with optimized design of directional strain response of three-sensor array is shown in Figure 3b. The structure of three-sensor array was confirmed as tri-angular form with tilting angle of 45° for omnidirectional sensing. In addition, the strain at the channels was analyzed as 33.5% (0°), 23% (45°), and 6.2% (90°), respectively at 30% strain intensity and 0°. Moreover, the FEA simulations for determining the strain limitation of optimized structure were presented in Figure S6, Supporting Information. By comparing the difference between the strain applied at the check points and the actual applied strain to the device, we can identify the possible responses according to the location of the applied strain. Overall, although from 5% (total difference for minimal actual strain of 4%) to 9.2% (for maximum actual strain of 28%), strain error can be detected in the present structure, the error rate and sensing limitation can be correspondingly diminished when much less device distance and device area is employed with more scaled-down array structures. Concretely, when the number of sensors is increased, more information about the direction and strain level can be acquired which can increase the detection range or improve the efficiency. On the other hand, the addressing time for measurement, energy consumption, and the footprint would increase as a trade-off. Accordingly, we choose the three-sensor array as an optimum device structure for our machine-learned omnidirectional strain sensor array.

After this, the static and dynamic sensing characteristics of fabricated strain sensor unit and sensor array were investigated under diverse strain conditions. Here, the sensing performance was evaluated by obtaining the relative change of resistance ($\Delta R/R_0$, ΔR = relative change of resistance, R_0 = initial resistance). In addition, the corresponding GF was calculated by GF = $(\Delta R/R_0)/\varepsilon$. At first, the static sensing characteristics were analyzed. As shown in **Figure 4**a, the sensor array consisting of three-unit sensors (sensor 1, 2, and 3) was stretched with strain directions of 0°, 45°, 90°, and 135°. With $\theta = 0°$, the channel of sensor 1 is parallel to the strain direction. Therefore, sensor 1 shows the highest resistance change. On the other hand, with the sensors 2 and 3, which are tilted by 45° and 90° with respect to the strain direction, respectively, the resistance variations

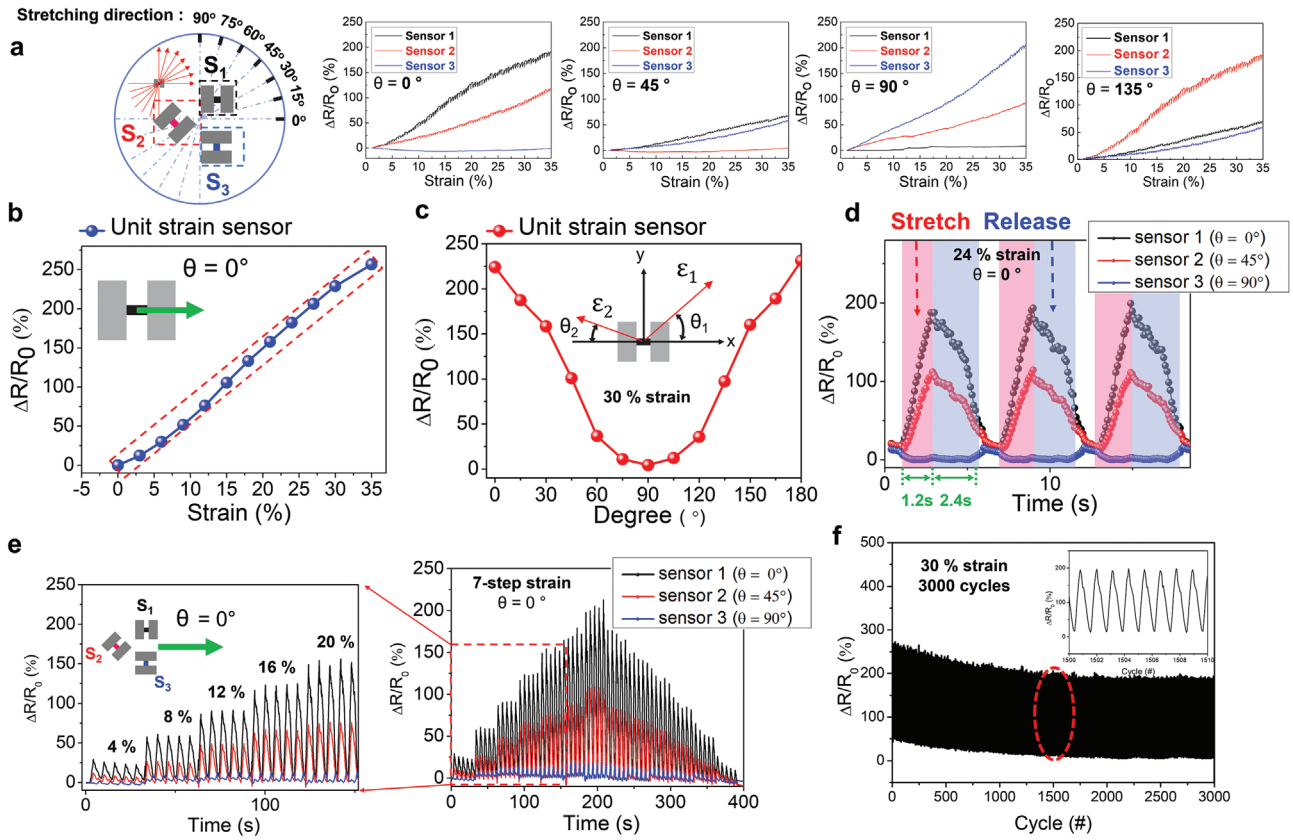

Figure 4. Analysis of static and real-time responses to various strain intensities and directions. a) Relative change of resistance ($\Delta R/R_0$) in the strain sensor array in the strain range of 0–35% at stretching angles of 0°, 45°, 90°, and 135°. b) Relative change of resistance of a unit sensor in the strain range of 0–35% ($\theta = 0°$). The corresponding gauge factor was ≈8. c) Relative change of resistance in the strain direction range of 0–180° (strain intensity = 30%). d) Real-time response characteristics of three-strain sensor array in the strain range of 0–24% ($\theta = 0°$). e) The variation of resistance when the strain was changed from 0% to 30% with seven steps ($\theta = 0°$). f) Stretching and releasing cyclic test data for 3000 cycles (30%, $\theta = 0°$) and the inset shows change of resistance at ≈1500–1508 cycles.

are relatively low. When $\theta = 45°$, sensors 1 and 3 show similar resistance change while sensor 2 shows almost no resistance change. Here, the channels of sensors 1 and 3 are 45° tilted with the strain direction, while the channel of sensor 2 is 90° to the strain direction. In addition, when $\theta = 90°$, the opposite trend is observed to those when $\theta = 0°$. Furthermore, with $\theta = 135°$, sensor 2 shows the highest resistance change because the channel of sensor 2 is parallel to the strain direction. However, for sensors 1 and 3, for which the channels are 45° tilted to the strain direction, the resistance variations are low. Additional results for various stretching directions from 0° to 180° with 15° step are summarized in Figure S7, Supporting Information, showing a similar dependency on the strain direction.

As shown in Figure 4b, the unit strain sensor showed decent sensitivity (GF ≈ 8), good linearity in the strain range of ≈0–35%. In fact, the GF of 8 can be considered as not very high sensitivity, while it is sufficient to be applied for an omnidirectional strain sensor array that can detect direction and strain level simultaneously. When the strain direction is changed, the resistance variation is changed accordingly. Figure 4c shows the relative change of resistance at different strain directions (≈0–180°, 15° step). As displayed, $\Delta R/R_0$ is decreased as the strain direction increases from 0° to 90°. In particular, the $\Delta R/R_0$ approaches almost to zero at 90° (transversal direction). Afterward, from 90° to 180°, $\Delta R/R_0$ increases symmetrically due to the uni-directional features of the sensor. The strain direction-dependent resistance variation can be clearly observed in three unit sensors having different tilting angles. Figure 4d shows the real-time response characteristics of three-unit sensors when stretched up to 24% at a rate of 1%/50 ms (strain/time) rate. It is observed that sensor 1 showes large resistance change. Meanwhile, sensor 2 shows relatively smaller resistance change and sensor 3 shows almost no change, indicating strain direction dependency. As described, the strain direction-dependent resistance variation can be attributed to less effective longitudinal strain which is applied to the sensor when θ is increased. Furthermore, the response time of the sensor was evaluated. The sensor showed rising time of ≈1.2 s and falling time of ≈2.4 s in the range of 10–90% change in resistance. The relatively longer falling time is attributed due to the intrinsic resilient properties of PDMS, requiring an extra time to completely return to the initial state.[24,33,34] Figure 4e shows the sensing response to various strain levels (ε = ≈0–20%). It is clear that each sensor shows proportional responses to strain in this strain region and different levels of resistance variation depending on the sensor rotation angle. At high strain levels, slight fluctuations in resistance change are observed. This is general phenomenon that occurs frequently in the elastomer base mixture and some fluctuations may occur depending on the measurement environment and the elastic recovery force during fast dynamic test.[25,35] However, in this study, ML is introduced to compensate for such fluctuation errors by using numerous datasets. In addition, for practical demonstrations, the first 100 cycles are considered as network stabilization period. At the beginning of the cycle, the network interconnection of nanoparticles and nanowires inside the mixture is stabilized. After that, the sensor device shows relatively good stability up to 3000 cyclic stretching and releasing test as shown in Figure 4f.[36]

Although the results show that the sensor array can identify the strain direction by comparing the responses of each sensor, it is not trivial to predict the strain intensity and direction when arbitrary strain stimulus is applied. This is due to many possible combinations of strain intensities and directions. To ensure the viability of the sensor array for identifying the strain, a condition classification neural network model is utilized. For the ML process; however, a large data point is needed to enhance the accuracy of learn-verifying process. Therefore, to generate more detailed strain direction-dependent data sets, we designed and implemented a sensor array consisting of seven-unit sensors as shown in Figure S8a, Supporting Information (each sensor tilted by 15°). First, to verify any variation of effective strain by increasing the number of sensors, FEA simulation was carried out for arrays having seven- and three-unit sensors. As shown in Figure S8a,b, Supporting Information, when the arrays were stretched by 30% along the x-axis ($\theta = 0°$), the strain applied at the channel of sensors was almost identical. For example, the strain applied on 0°-sensor in seven-sensor array was 33.8%, which is similar to that observed in 0°-sensor in the three-sensor array (33.5%). In addition, the strain applied on 45°- and 90°-sensors was also similar. The slightly higher strain observed in 90°-sensor in the seven-sensor array (7.3%) can be attributed to the configuration of sensor arrangement. In particular, the seven-sensor array has larger gaps between the sensors and because the electrode regions are relatively rigid, larger strain is applied to the sensing channel compared to the three-sensor array. More specific validation of data compatibility between seven-sensor and three-sensor arrays is demonstrated in Figure S9, Supporting Information. Nevertheless, using the seven-sensor array configuration, more detailed 75 000 data points for ML are acquired with various strain directions and intensities with almost similar trends (Figure S9a,b, Supporting Information). Furthermore, statistical data (from 25 samples) was added to ensure the uniformity over the number of devices. The 25 sensors average relative change of resistance versus strain up to 35% at 0° with error bars is calculated and shown in Figure S10c, Supporting Information. Last, the examples of input data corresponding to specific situations (8%, 0° and 24%, 135°) are provided in Figure S11, Supporting Information.

Aforementioned, a method that enables omnidirectional strain perception by utilizing ML process is strongly needed to accurately identify both the direction and intensity of strain. Among various ML models and algorithms developed for prediction and classification of cross-reactive stimuli, we adopted the multi-class/multi-output neural network model which is typically used in multi-way classification process.[5,37,38] **Figure 5**a shows the neural network structure of direction and strain level perception using ML-based classification algorithms. Owing to the distinct target of strain intensity and direction, the multi-class/multi-output classification algorithm is examined. This algorithm is typically used for multiple classification problems with multiple categories. For this process, continuous value of resistance from three-strain sensors for 5 s (3-sensors × 60 points = 180 data points) are used as the input dimension and the direction-dependent strain (angle-strain) data samples are adapted as target (output) in the forms of one hot encoding to the algorithm. For the training process, a total of 75 000 data points (from real measurement) are used, and among them, 25 000 data points

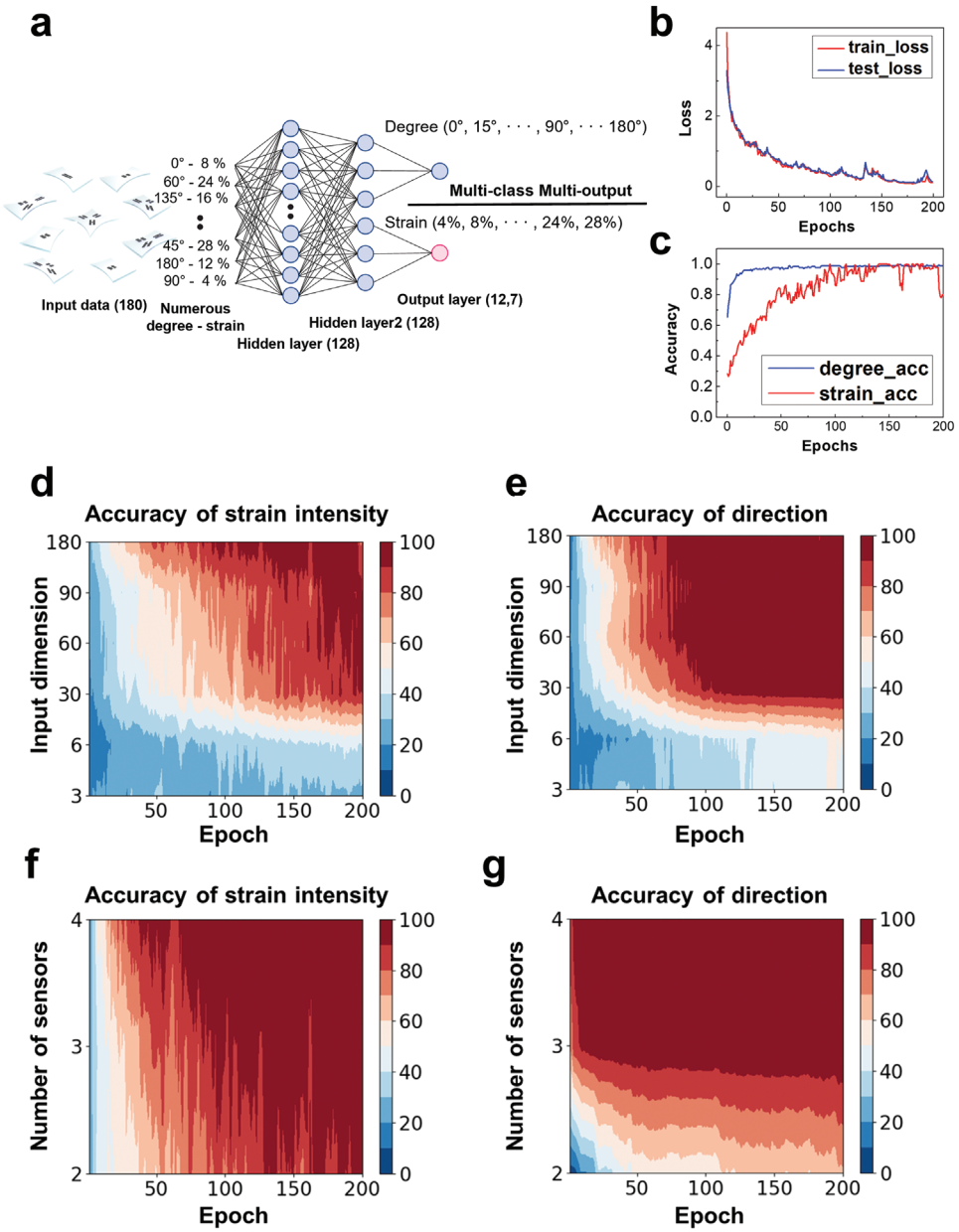

Figure 5. Cognition of the direction and strain process using the classification model for ML. a) Schematic of ML process with enormous input sensor data and multi-class neural network flow. b) The training and test loss function characteristics versus epochs up to 200; the corresponding train loss was 0.101 and test loss was 0.132. c) The accuracy characteristics versus epochs up to 200, the corresponding accuracy of degree and strain are analyzed over 90% after 100 epochs. d–g) Visualized synaptic weight contour maps for accuracy of detecting direction/strain intensity (*z*-axis color legend) versus training epochs (*x*-axis) and input dimension data / number of sensors (*y*-axis). (d,e) are the contour maps with input dimension data in a three-sensor array device. (f,g) are the contour maps with number of sensor array (two-sensor array with 120-dimension, three-sensor array with 180-dimension, and four-sensor array with 240-dimension).

are applied for the verification. Then, two hidden layers (each layer consist of 128 neurons) and two output layers for direction and strain level are constructed and the targets are derived in the forms of (12, 7) indicating 12-angle (from 0° to 180°) and 7-strain (from 0% to 28%), respectively. In the learning and verifying process, the cross entropy is used as loss function as:

$$\text{Loss: } \sum_{i=1}^{n_1} t_i \log(y_i) + \sum_{k=1}^{n_2} t_k \log(y_k) \tag{2}$$

where "*i*" is each class of strain, "*k*" is each class of degree, thus, $n_1 = 7$, $n_2 = 12$ (4% strain, 8% strain .... 28% strain, and, 0°, 15° .... 90° .... 175°), "*t*" is the true value, "*y*" is the probability that the class is "*i*" or '*k*' when the model predicts. (SoftMax outputs).[39] Furthermore, the Adam optimizer in PyTorch library, a convex optimization method with a momentum strategy which is utilized to adjust the learning direction and step size appropriately and reduce the loss between actual results and predicted results in neural network is adapted in this process.[40,41]

The more detailed neural-network architecture is illustrated in Figure S12, Supporting Information. As shown in Figure 5b, cross entropy loss in the training set was 0.101 after 200 epochs and test set loss function was 0.132 after 200 epochs. In ML, the accuracy and time efficiency are important parameters which show the predictability, efficiency, and reliability of developed algorithm. Therefore, we tried to obtain high accuracy and short training + verifying time by changing the input and output dimensions and the structure of the hidden layer. The details are described in Figure S13, Supporting Information. As a result, the accuracy for identifying the direction was over 98.6% after 30 epochs and the strain intensity was 96.4% in average after 100 epochs (Figure 5c) and the training + verifying time was 3.35 s These results are important indicators to show that developed ML process is well-optimized and enables the detection of an arbitrary strain/direction with high accuracy. Figure 5d–f shows the weight contour map of cognitively learned omnidirectional sensor array indicating trained accuracy tendency of strain intensity/direction (*z*-axis color legend) corresponding to training epoch (*x*-axis) and the input dimension/number of sensors (*y*-axis).[42,43] Of course, as the training epochs increase, the accuracy increases because the loss decreases by the algorithm. In addition, it is confirmed that the accuracy increases as the input dimension increases in both cases of strain intensity and direction. At last, as the number of sensors increases, the accuracy of strain intensity/direction tends to increase. For accuracy of strain intensity, the accuracy increases in proportion to the number of sensors, but after about 100 epochs, the accuracy of the three-sensor array is almost same with those of larger number sensor arrays. In the case of the two-sensor array, as described in the manuscript, the accuracy of direction is very low possibly due to the limited directional sensing properties with the two sensors. As a result, like other classification models, the accuracy of developed algorithm about direction and strain intensity has increased following diverse parameters such as training epochs, number of sensors, and the input dimension. In addition, the confusion matrix is shown in Figure S14, Supporting Information. These results show both the direction and strain intensity of the verifying data are accurately predicted with a very high probability of ≈98% ± 2% under most conditions. Furthermore, the accuracies corresponding to the number of unit sensors such as three-sensor structure and two-, four-sensor structure and the diverse input dimension are also compared in Figure S15, Supporting Information. Accuracy for direction represents a value about whether it can recognize and classify direction of strain ranging from 0° to 360°, and intensity of strain from 0% to 28%. Compared to the three-sensor array, the accuracy of a two-sensor array is relatively lower. In particular, the accuracy for strain direction is ≈60%. This low accuracy indicates that the two-sensor array can only recognize directions from 0° to 90°, not up to 180°. In addition, the accuracy of a four-sensor array is relatively high. The accuracy for strain direction is 100% and for strain intensity is 99.2%. As the number of sensors increases, more data on a more detailed information about direction and strain intensity can be obtained, which can lead to improved accuracy. However, the difference between three- and four-sensor array in terms of the prediction accuracy is ≈2% on average. Therefore, even with three-sensors, detection and prediction of both direction and strain intensity are possible with high accuracy and efficiency. These results show that the three-sensor array is an optimized compact architecture that can accurately recognize omnidirectional strain. In conclusion, the sensitivity of this proof-of-conceptual omnidirectional strain sensor is likely not enough to accomplish the role of human skin sense; however, as a result of implementing comprehensive system including neural network with soft sensor engineering, the average accuracy for detecting both strain intensity and direction is over 96%. Therefore, we envision that more scaled-down proof-of-concept device with ML-based approach can provide a versatile way to advance the e-skin systems with reduced architecture complexity and enhanced adaptability to direction with strain beyond the limitation of conventional one-way strain sensor system.

To validate the viability of cognitively learned omnidirectional strain sensor array, arbitrary stretching tests are carried out. First, as shown in **Figure 6**a, a 28% strain ($\theta = 0°$), which is manually measured with ruler, is applied. The reason is that the manually applied strain can be accurately predicted in this test because the algorithm calculates an approximation by dividing the angle (≈0–180°) and intensity (≈0–30%) into 12 and 7 steps during the training process, respectively. In other words, the closest direction is determined among the degrees of 0, 15°, ... 90°, ..., and 180° by analyzing the resistance change values from the three sensors. In addition, strain intensity prediction shows ca. ±2% margin error because the strain values can be predicted with 7-step (28%/7 = 4%). For example, when a strain intensity in the range of ≈26–30% is applied, it is analyzed as 28% by the classification algorithm. Figure 6a (right) shows the resistance change of three-sensor array when manually stretched by 28% and $\theta = 0°$. The sensor 1 exhibits the highest change in resistance because the strain is applied in parallel to the channel deriving maximum principal strain. In addition, sensors 2 and 3 show the response to the stretching/releasing tilted by 45° and 90°, respectively at 28% of strain intensity. As their dynamic characteristics are iterative and stable, the manually stretched condition is accurately recognized by the algorithm as 28% of strain at 0°. Second, the sensor array is attached to a stick balloon, and then, air is injected as shown in Figure 6b.

Afterward, the dataset of second region in the graph, which indicates typical characteristics, is used as an input data to the algorithm. Sensor 1 shows almost no change in resistance because the effective strain is close to perpendicular to channel layer (90°). However, the resistance of sensors 2 and 3 changes in proportion to $\varepsilon_x = \varepsilon \times cos^2\,\theta$, following the air injection. Consequently, the output shows 90°, 20% of strain intensity, which is the same result as the input stimulus. Last, the sensor array is attached to a round balloon and air is injected. In this case, we can expect the surface of balloon to be stretched omnidirectionally; therefore, the sensors exhibit almost same responses. As shown in Figure 6c (right), resistance variations of the sensors 1 and 2 are almost identical and sensor 3 also shows similar characteristics although the value is slightly low that is negligible because it is within marginal error of resistance change in algorithms. Consequently, the algorithm interprets these results as omnidirectional stretching direction with strain intensity of 20%.

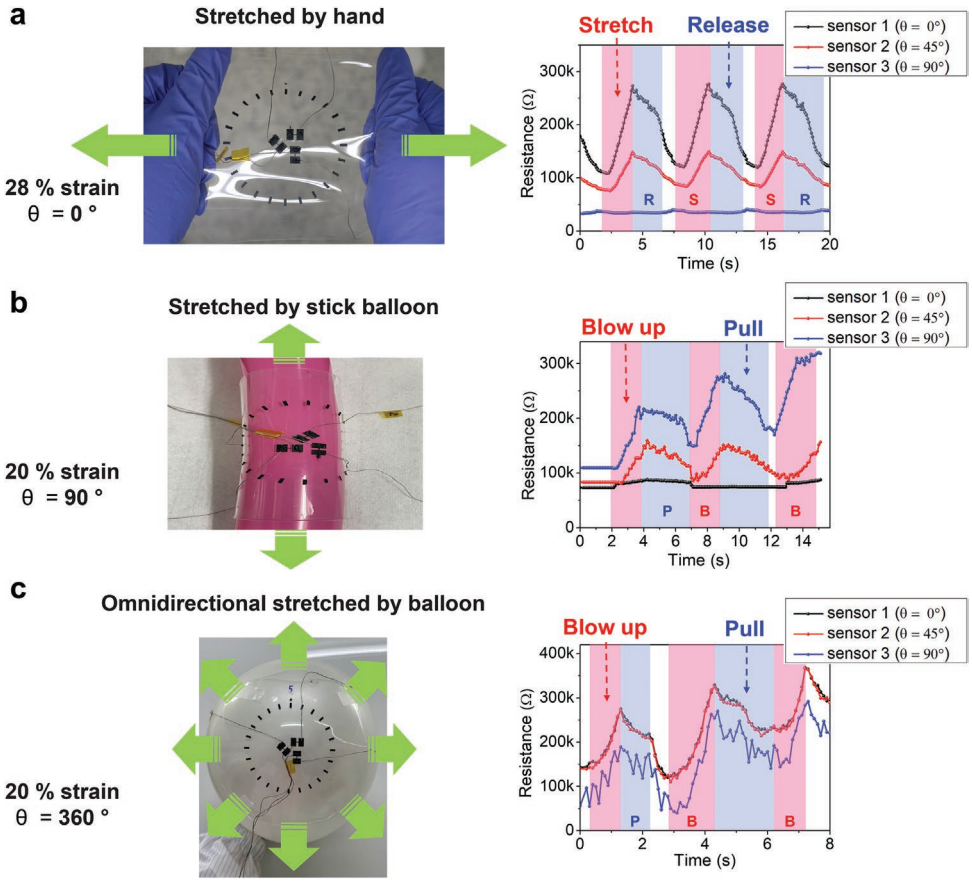

Figure 6. Omnidirectional strain perception via cognitive learning algorithm. a) The photograph of arbitrary stretching test by hand and the result graph of strain sensor array. b) The photograph of stretching test attached to stick balloon and the result graph with blowup and pull process of strain sensor array. c) The photograph of stretching test attached to normal balloon and the result graph with blowup and pull process of strain sensor array.

3. Conclusions

We have demonstrated omnidirectional strain perceptible sensor array with cognitively learned neural networks for accurate recognition of arbitrary strain with variable intensity and direction. The strain information is obtained by the heterogeneous surface featured strain sensor array and the directional distribution of arbitrary strain forces are inferred by ML-based neural networks. The insight has an overall strain intensity and direction accuracy ≈98 ± 2% over a strain range of ≈0–30% in various surface stimuli environments. The hardware and software design concepts reported here imply that the cognitively learned stretchable strain sensor array can offer a general route to realize highly sensitive, extremely reliable stimulation perception with a marginal device complexity and implementation for large-scaled applications.

4. Experimental Section

Fabrication of MWCNT/CB-PDMS Composite for Electrodes and Channel: For the fabrication of MWCNT/CB-PDMS composite, MWCNT (LUCAN BT1001M from LG Chem, 10 nm of diameter and 250 m^2 g^{-1} surface area) and CB nanoparticles (Denka Black from Denka, 0.25 g cm^{-3} bulk density and under 0.001% of 45 µm sieve) were mixed with 1: 1 in weight. Then, the mixture was dispersed in PDMS with the ratio of 10 wt% between MWCNT/CB composite and PDMS by using ball mill process in a ceramic container (300 rpm, 3 h). In the middle of mixing, viscosity and dispersion were checked frequently. Then, the ratio of PDMS base to curing agent was 10:1 in weight. Last, the MWCNT/CB-PDMS composite was aged in air for 1 h to stabilize the percolation networks.[2,44]

Fabrication of Omnidirectional Strain Perceptible Sensor Array: At first, a PDMS sheet was prepared with thickness of 0.5 mm. On the PDMS, PET film (3 mm × 6 mm, 70 µm) was attached by using a silicone paste (Dragon skin 30, Smooth-On). Then, PDMS was spin-coated on the substrate to make a flat surface moulding the rigid island. Next, to fabricate the sensor array, the MWCNT/CB-PDMS mixture was printed on the PDMS substrate using a shadow mask followed by contact with conductive fibers (silver coated conductive yarn, Soitex) for evaluating the strain sensor array. Last, the sensor array was cured at 90° for 2 h. The size of sensor unit was 7.5 mm × 6 mm and the size of the omnidirectional strain sensor array was 20 mm × 15 mm.

Finite Element Analysis (FEA) of the Strain Sensor Array: To investigate the strain distribution of the sensor array and the operation mechanism, FEA simulation was carried out (COMSOL Multiphysics 5.5). Hexahedron PDMS was designed with nanofiller composite in the actual array size and structure with three-sensor array and seven-sensor array. The strain was applied by using Prescribed Displacement (from 0% to 60%) in Solid Mechanics and analyzed by First Principal Strain in the results tap. The designed model and the material parameters used for the simulation are listed in Table S1, Supporting Information.

Analyses of Strain Sensing Characteristics: The electrical resistance of MWCNT/CB-PDMS-based strain sensor was measured by using a resistance-meter (2604B, Keithley). The response and relaxation time

were determined and analyzed as the minimum time from initial state to target strain level using the cyclic stretchable measurement equipment (SSMS21, TERALEATHER). For the dynamic measurement of the sensor array, a measuring system comprised of a source meter (2604B, Keithley) and a homemade stretching jig connected to a data acquisition system (DAQ; TERALEATHER) was used.

Data Preparation and Process for ML: Multiclass-multioutput classification model was used to perceive the direction and intensity of strain. To apply the classification model for the perception of direction and strain simultaneously, a total of 75 000 data points were used and among them, 25 000 data points were used for the verification. All training data and test data did not overlap, and all data points were obtained by real measurement. Then, the algorithm made hidden layers (128–128) to reduce the loss function by the Adam optimizer. The ML process was conducted using Python.

Supporting Information

Supporting Information is available from the Wiley Online Library or from the author.

Acknowledgements

J.H.L., S.H.K., and J.S.H. contributed equally to this work. This work was supported by the Institute of Information & Communications Technology Planning & Evaluation (IITP) grant funded by the Korea government (MSIT) (2017-0-00048), the Development of Core Technologies for Tactile Input/Output Panels in Skintronics (Skin Electronics), and 2022-0-00020, Imperceptible On-Skin Sensor Devices for Musculoskeletal Monitoring and Rehabilitation. In addition, this research was supported by the Chung-Ang University Graduate Research Scholarship in 2018.

Conflict of Interest

The authors declare no conflict of interest.

Data Availability Statement

The data that support the findings of this study are available from the corresponding author upon reasonable request.

Keywords

direction recognition, machine learned strain sensors, omnidirectional strain sensors, strain sensor, stretchable electronics

Received: September 6, 2022
Revised: December 20, 2022
Published online:

[1] N. Gogurla, B. Roy, J. Y. Park, S. Kim, *Nano Energy* **2019**, *62*, 674.
[2] Y. Gao, S. Gu, F. Jia, G. Gao, *J. Mater. Chem. A* **2020**, *8*, 24175.
[3] Y. Wang, S. Lee, T. Yokota, H. Wang, Z. Jiang, J. Wang, M. Koizumi, T. Someya, *Sci. Adv.* **2020**, *6*, eabb7043.
[4] J. S. Heo, K. W. Lee, J. H. Lee, S. B. Shin, J. W. Jo, Y. H. Kim, M. G. Kim, S. K. Park, *Micromachines* **2020**, *11*, 1103.
[5] J. H. Lee, J. S. Heo, Y. J. Kim, J. Eom, H. J. Jung, J. W. Kim, I. Kim, H. H. Park, H. S. Mo, Y. H. Kim, S. K. Park, *Adv. Mater.* **2020**, *32*, 2000969.
[6] X. Xu, Y. Chen, P. He, S. Wang, K. Ling, L. Liu, P. Lei, X. Huang, H. Zhao, J. Cao, J. Yang, *Nano Res.* **2021**, *14*, 2875.
[7] X. Wang, X. Liu, D. W. Schubert, *Nano-Micro Lett.* **2021**, *13*, 64.
[8] R. Nur, N. Matsuhisa, Z. Jiang, M. O. G. Nayeem, T. Yokota, T. Someya, *Nano Lett.* **2018**, *18*, 5610.
[9] F. Li, Y. Liu, X. Shi, H. Li, C. Wang, Q. Zhang, R. Ma, J. Liang, *Nano Lett.* **2020**, *20*, 6176.
[10] D. J. Lipomi, M. Vosgueritchian, B. C.-K. Tee, S. L. Hellstrom, J. a Lee, C. H. Fox, Z. Bao, *Nat. Nanotechnol.* **2011**, *6*, 788.
[11] T. Yamada, Y. Hayamizu, Y. Yamamoto, Y. Yomogida, A. Izadi-Najafabadi, D. N. Futaba, K. Hata, *Nat. Nanotechnol.* **2011**, *6*, 296.
[12] W. Feng, W. Zheng, F. Gao, X. Chen, G. Liu, T. Hasan, W. Cao, P. Hu, *Chem. Mater.* **2016**, *28*, 4278.
[13] K. K. Kim, S. Hong, H. M. Cho, J. Lee, Y. D. Suh, J. Ham, S. H. Ko, *Nano Lett.* **2015**, *15*, 5240.
[14] G. Choi, H. Jang, S. Oh, H. Cho, H. Yoo, H. Il Kang, Y. Choi, S. H. Kim, H. S. Lee, *J. Mater. Chem. C* **2019**, *7*, 9504.
[15] J. H. Lee, J. Kim, D. Liu, F. Guo, X. Shen, Q. Zheng, S. Jeon, J. K. Kim, *Adv. Funct. Mater.* **2019**, *29*, 1901623.
[16] Q. Hua, J. Sun, H. Liu, R. Bao, R. Yu, J. Zhai, C. Pan, Z. L. Wang, *Nat. Commun.* **2018**, *9*, 244.
[17] H. Li, J. Chen, X. Chang, Y. Xu, G. Zhao, Y. Zhu, Y. Li, *J. Mater. Chem. A* **2021**, *9*, 1795.
[18] L. Ma, W. Lu, *Mater. Lett.* **2020**, *260*, 126959.
[19] S. Wang, H. Ning, N. Hu, Y. Liu, F. Liu, R. Zou, K. Huang, X. Wu, S. Weng, Alamusi, *Adv. Mater. Interfaces* **2020**, *7*, 1901507.
[20] S. Ota, A. Ando, D. Chiba, *Nat. Electron.* **2018**, *1*, 124.
[21] S. M. Kwon, J. Y. Kwak, S. Song, J. Kim, C. Jo, S. S. Cho, S. Nam, J. Kim, G. Park, Y. Kim, S. K. Park, *Adv. Mater.* **2021**, *33*, 2105017.
[22] M. Wang, T. Wang, Y. Luo, K. He, L. Pan, Z. Li, Z. Cui, Z. Liu, J. Tu, X. Chen, *Adv. Funct. Mater.* **2021**, *31*, 2008807.
[23] S. Gong, W. Schwalb, Y. Wang, Y. Chen, Y. Tang, J. Si, B. Shirinzadeh, W. Cheng, *Nat. Commun.* **2014**, *5*, 3132.
[24] H. Shen, H. Ke, J. Feng, C. Jiang, Q. Wei, Q. Wang, *Nanomaterials* **2021**, *11*, 2333.
[25] M. Li, S. Chen, B. Fan, B. Wu, X. Guo, *Adv. Funct. Mater.* **2020**, *30*, 2003214.
[26] G. Yang, X. Tang, G. Zhao, Y. Li, C. Ma, X. Zhuang, J. Yan, *Chem. Eng. J.* **2022**, *435*, 135004.
[27] K. T. S. Kong, M. Mariatti, A. A. Rashid, J. J. C. Busfield, *Polym. Bull.* **2012**, *69*, 937.
[28] J. Jin, X. Wang, S. Di, W. Lin, H. Bi, J. Zhang, *Microelectron. Eng.* **2021**, *247*, 111586.
[29] M. Amjadi, A. Pichitpajongkit, S. Lee, S. Ryu, I. Park, *ACS Nano* **2014**, *8*, 5154.
[30] J. H. Kong, N. S. Jang, S. H. Kim, J. M. Kim, *Carbon* **2014**, *77*, 199.
[31] Z. Wang, Y. Wang, Y. Chen, M. Yousaf, H. Wu, A. Cao, R. P. S. Han, *Adv. Funct. Mater.* **2019**, *29*, 1807467.
[32] Y. Zheng, Y. Li, K. Dai, Y. Wang, G. Zheng, C. Liu, C. Shen, *Compos. Sci. Technol.* **2018**, *156*, 276.
[33] L. Liu, S. Niu, J. Zhang, Z. Mu, J. Li, B. Li, X. Meng, C. Zhang, Y. Wang, T. Hou, Z. Han, S. Yang, L. Ren, *Adv. Mater.* **2022**, *34*, 2200823.
[34] W. C. Gao, W. Wu, C. Z. Chen, H. Zhao, Y. Liu, Q. Li, C. X. Huang, G. H. Hu, S. F. Wang, D. Shi, Q. C. Zhang, *ACS Appl. Mater. Interfaces* **2022**, *14*, 1874.
[35] J. Lee, S. Pyo, D. S. Kwon, E. Jo, W. Kim, J. Kim, *Small* **2019**, *15*, 1805120.
[36] Y. Ding, J. Yang, C. R. Tolle, Z. Zhu, *RSC Adv.* **2016**, *6*, 79114.
[37] B. Polat, L. L. Becerra, P. Y. Hsu, V. Kaipu, P. P. Mercier, C. K. Cheng, D. J. Lipomi, *ACS Appl. Nano Mater.* **2021**, *4*, 8126.
[38] Y. Jiang, A. Sadeqi, E. L. Miller, S. Sonkusale, *Sci. Rep.* **2021**, *11*, 2646.
[39] P. T. De Boer, D. P. Kroese, S. Mannor, R. Y. Rubinstein, *Ann. Oper. Res.* **2005**, *134*, 19.

[40] a) R. Nishihara, L. Lessard, B. Recht, A. Packard, M. I. Jordan, *Proc. 32nd Int. Conf. on Machine Learning* **2015**, *37*, pp. 343–352; b) S. Mehta, C. Paunwala, B. Vaidya, *2019 Int. Conf. on Intelligent Computing and Control Systems (ICCS)*, IEEE, Piscataway, NJ, USA **2019**, pp. 1293–1298.

[41] a) G. Taylor, R. Burmeister, Z. Xu, B. Singh, A. Patel, T. Goldstein, in *Proc. 33nd Int. Conf. on Machine Learning* **2016**, *48*, pp. 2722–2731; b) S. Bock, M. Weis, in *2019 Int. Joint Conf. on Neural Networks (IJCNN)*, IEEE, Piscataway, NJ, USA **2019**, https://doi.org/10.1109/ijcnn.2019.8852239.

[42] C. Bachmann, T. Tetzlaff, R. Duarte, A. Morrison, *PLoS Comput. Biol.* **2020**, *16*, e1007790.

[43] F. Zhao, C. Lei, Q. Zhao, H. Yang, G. Ling, J. Liu, H. Zhou, H. Wang, *Mater. Today Commun.* **2022**, *30*, 103138.

[44] J. Lee, S. Shin, S. Lee, J. Song, S. Kang, H. Han, S. Kim, S. Kim, J. Seo, D. Kim, T. Lee, *ACS Nano* **2018**, *12*, 4259.